18

Analysis of Microparts Dynamics Fed Along on an Asymmetric Fabricated Surface with Horizontal and Symmetric Vibrations

Atsushi Mitani[1] and Shinichi Hirai[2]
[1]*Department of Design, Sapporo City University*
[2]*Department of Robotics, Ritsumeikan University*
Japan

1. Introduction

Devices to feed along microparts, such as ceramic chip capacitors and resistors, have become more common, due to their use in sorting, inspecting, and shipping mass produced microparts. In microparts feeding, to feed along microparts in one direction, the driving force applied to each micropart must vary according to the direction of motion of the micropart. Especially, the motion of microparts smaller than submillimeter can be affected by not only inertia but also adhesion which is caused by electrostatic, van der Waal's, intermolecular forces, and surface tension.

Now we have developed a novel microparts feeder applied an asymmetric fabricated surface, for example, sawtoothed surface, as a feeder table (Figure 1) (Mitani, 2006). The asymmetric fabricated surface can feed along microparts in one direction using horizontal and symmetric vibrations because contact between a micropart and the asymmetric fabricated surface varies according to the direction of motion. In order to formulate the dynamics of micropart, we need to analyse driving force and adhesion according to these contacts.

In this chapter, we developed micropart dynamics considering the effect of contact. Sawtoothed silicon wafers with various pitch were applied for feeder table, and also 0603 (size, 0.6 x 0.3 x 0.3 mm: weight, 0.3 mg) capacitors were applied for microparts.

First, we analysed contact between a micropart and a sawtoothed surface. Each surface profile model was approximated by a linear polynomial based on measurements using a microscopy system.

Secondly, we derived dynamics including the effect of adhesion. We analysed contact between both approximated models, because both inertia caused by feeder vibrations and adhesion vary according to contact. Supposing that adhesion occurs in the direction vertical to the tangent and also adhesion acts when the distance between two surface models is smaller than an adhesion limit, we obtained an adhesion model. Then the adhesion model parameters were identified using the results of friction angle measurement experiments of microparts.

Finally, we assessed the dynamics derived above. We firstly conducted feeding experiments of microparts using various pitch of sawtoothed surface with the same driving and

environmental conditions. Using these experimental results, we verified driving condition and feeding velocity at each sawtooth pitch, and also we assessed an appropriate driving condition and a feeder surface. Feeding simulations were then executed using dynamics derived with the same parameters as the feeding experiments. These simulation results were compared with experimental results in order to evaluate the derived dynamics.

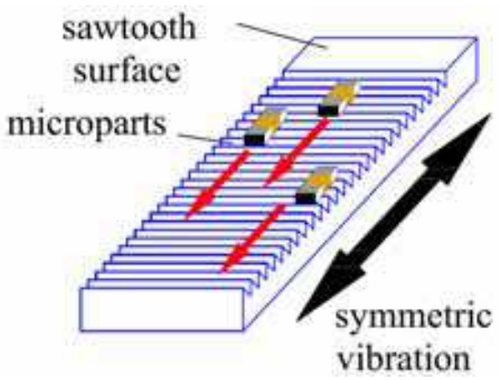

Fig. 1. Diagram of microparts feeding using a sawtoothed surface with symmetric vibrations

2. Related works

Partsfeeder is a key device in factory automation. The most popular feeders are vibratory bowl feeders (Maul, 1997), which use revolving vibrators to move parts along a helical track on the edge of a bowl. Linear feeders as well as an inclined mechanism and oblique vibration for unidirectional feeding (Wolfsteiner, 1999), have also been developed. In all of these systems, the aspect ratio of the horizontal/vertical vibrations must be adjusted to prevent parts from jumping. In our system, however, this adjustment is not necessary because only horizontal vibration is used.

A parts feeding that employs non-sinusoidal vibrations (Reznik, 2001) has been developed. The part moves to its target position and orientation or is tracked during its trajectory by using the difference between the static and sliding friction. Our system realizes unidirectional feeding by symmetric vibration of a sawtoothed surface, which yields different contact forces in the positive and negative directions.

Designing have been tested by simulation (Berkowitz, 1997 & Christiansen, 1996). The focus was mainly on the drive systems such as the structure and actuator, the movement of fed parts was generally neglected. In contrast, the movement of the microparts are considered in the present study.

Attempts have been made to improve the drive efficiency by feedback control systems (Doi, 2001) and nonlinear resonance systems (Konishi, 1997). Our system depends only upon contact between the feeder surface and the micropart. So the driving system is simple and uses an open loop system for feeding.

Micro-electro-mechanical systems (MEMS) technology has been used to mount on a planar board arrays of micro-sized air nozzles which, by turning on or off their air flow, have been used to control the direction of moving microparts (Fukuta, 2004 & Arai, 2002).

It is possible to perform manipulation with ciliary systems (Ebefors, 2000) and vector fields (Oyobe, 2001) without sensors. In this case, there are many actuator arrays on a vibratory plate. Actuator arrays enable control of contact between the vibratory plate and micropart in

order to accomplish the target manipulation. However, these studies did not mention the dynamics of the micropart, especially the effects of adhesion forces on its motion. Other various feeding systems using electric-field (Fuhr, 1999), magnetic (Komori, 2005), bimorph piezoelectric actuators (Ting, 2005), and inchworm systems (Codourey, 1995) have been developed. These studies, however, have also not investigated the contact between the feeder surface and the micropart.

3. Measurement tool

For inspection of both the sawtooth surface and the micropart surface profiles, we used the AZ-100 multi-purpose zoom microscopy system (Nikon Instech Co., Ltd.) (Figure 2), which includes a mono zoom optical system that enables on-axis observation and documentation and built-in optics of up to 8 times magnification. In combination with an objective lens of 5 times magnification, we could take pictures at up to 40 times magnification. This microscope also has an automatic stage driven by a stepping motor to control focus height at a resolution of 0.54 μm.

A digital camera is attached to the top of the microscopy system, and captured pictures were forwarded to a computer via USB interface, and saved as bitmap files. The resolution of forwarded pictures taken at 40 times magnification was 0.276 μm/pixel. We used the DynamicEye Real focus image synthesizing software (Mitani Corp.) to analyse these surface profiles. This software can synthesize a three dimensional (3D) model from these pictures according to focus height. Sections of the 3D model are analysed to obtain a surface profile model.

Fig. 2. AZ-100 multi-purpose zoom microscope (Nikon Instech Co., Ltd.)

4. Analysis of micropart surface

4.1 Detail of micropart

We applied a 0603 ceramic chip capacitor, electronic parts used in various mobile devices, as a micropart. As shown in Figure 3, a capacitor consists of a conductor and electrodes with convexities on each end surface. We obtained representative contours along a capacitor using a Form Talysurf S5C sensing-pin surface measurement tool (Taylor Hobson Corp.) (Figure 4). Electrodes contact the feeder because they protrude 10 μm higher than the conductor. To obtain minute profile models of these electrodes, we used the microscopy system mentioned above.

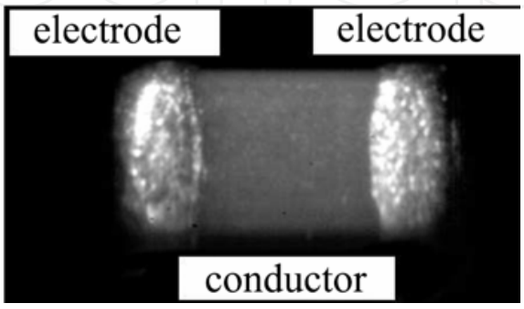

Fig. 3. Ceramic chip capacitor 0603 (size, 0.6 x 0.3 x 0.3 mm: weight, 0.3 mg)

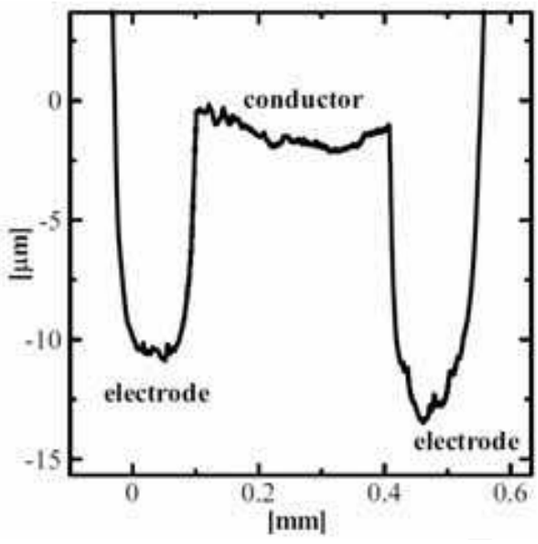

Fig. 4. Section of 0603 capacitor

4.2 Surface model of micropart based on measurements

Using the automatic capture mode of the DynamicEye Real software, we obtained a 3D model of an electrode shown in Figure 5 synthesized from 256 successive pictures with an interval of 0.54 μm in focus height at 40 times magnification. Analysing this 3D model, a numerical model of surface profile at any section was obtained. Figure 5 shows a profile model with a section along the y axis, and also Figure 6 shows a section along the x axis in Figure 4.

Next, we considered a convexity model on the surface of electrode. We assumed that only some higher convexities can contact the sawtoothed feeder surface. We then selected five convexities numbered from #1 to #5 in Figure 6 and 7. Let us approximate each convexity with a second order polynomial as follows:

$$y_p = b' x_p^{\,2} + c_p, \tag{1}$$

where, c_p is constant, y_p is defined along the vertical line, and also x_p is defined along the horizontal line. Figure 8 shows the profile model of the convexity #1 and its approximation function. Assuming that each approximation function could be rotated around the horizontal line, and be transformed to its minimum value at the position $(x_p, y_p) = (0,0)$ without loss of generality, equation (1) can be rewritten as:

$$y_p = b x_p^{\,2}, \tag{2}$$

where, $b \equiv -b'$. Averaging five transformed approximation functions, the coefficient was formulated as $b = 0.186$ (Figure 9).

Finally, the surface profile model of electrode convexity was defined by a hyperboloid of revolution of equation (2) around the y_p axis. When considering the z_p axis perpendicular to the $x_p - y_p$ plane with passing the position $(x_p, y_p) = (0,0)$, the trajectory of a point (x_p, y_p) on equation (2) was represented as a circle with a radius r as follows:

$$r = x_p = \sqrt{\frac{y_p}{b}}. \tag{3}$$

Then, the convexity surface model was formulated as:

$$x_p^{\,2} + z_p^{\,2} = y_p. \tag{4}$$

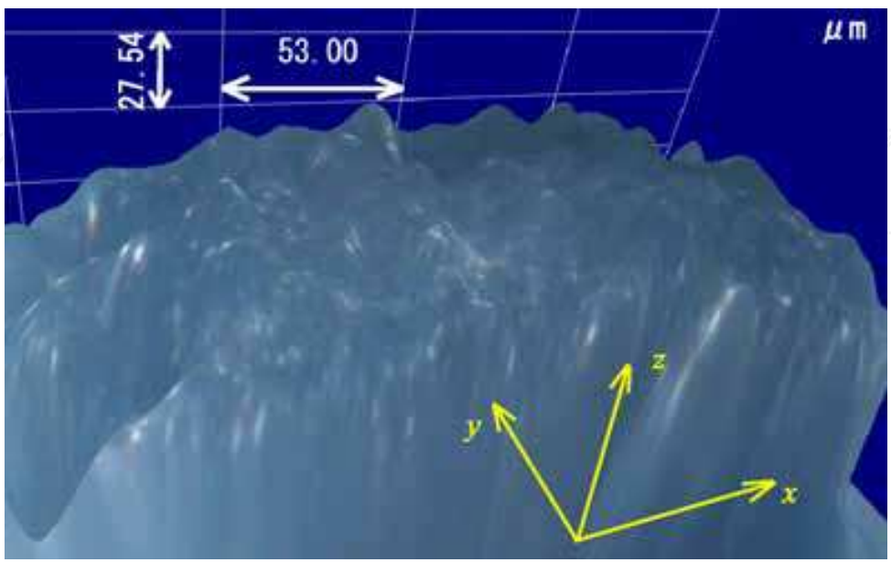

Fig. 5. Synthesized model of capacitor electrode

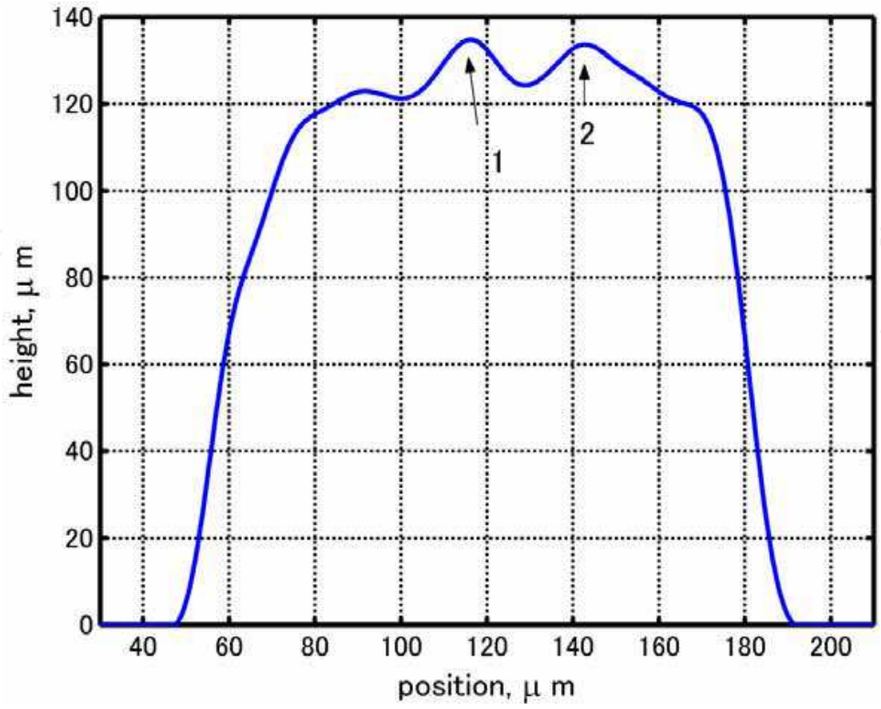

Fig. 6. Profile model along the y axis

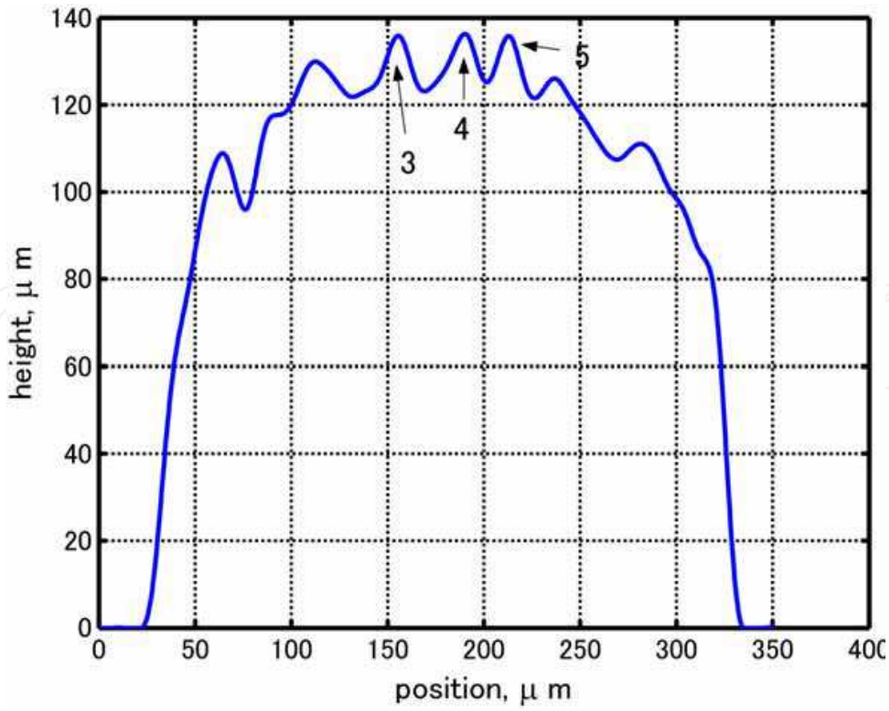

Fig. 7. Profile model along the x axis

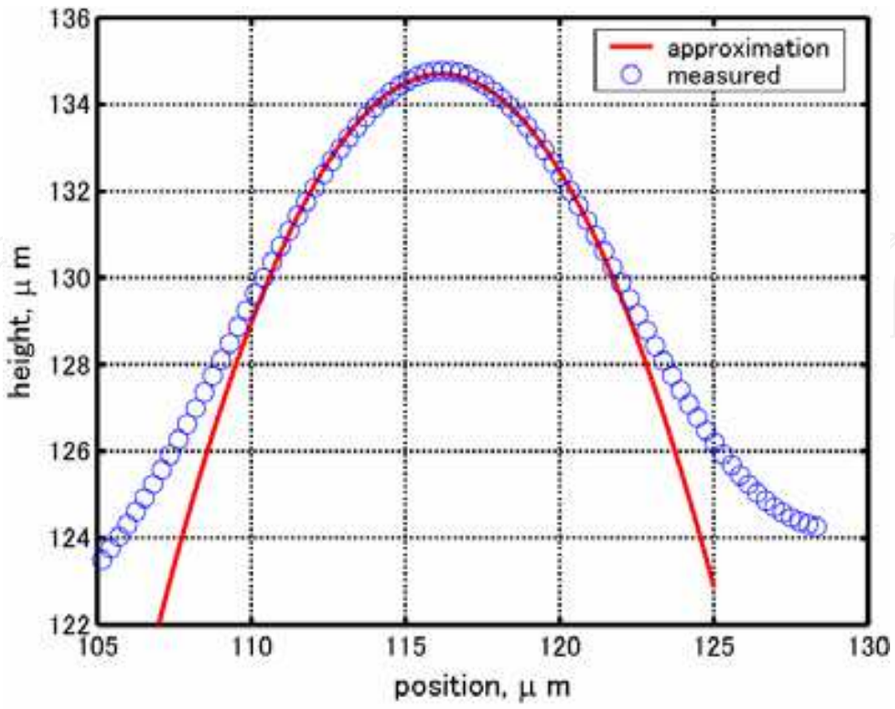

Fig. 8. Profile model of convexity #1 and its approximation

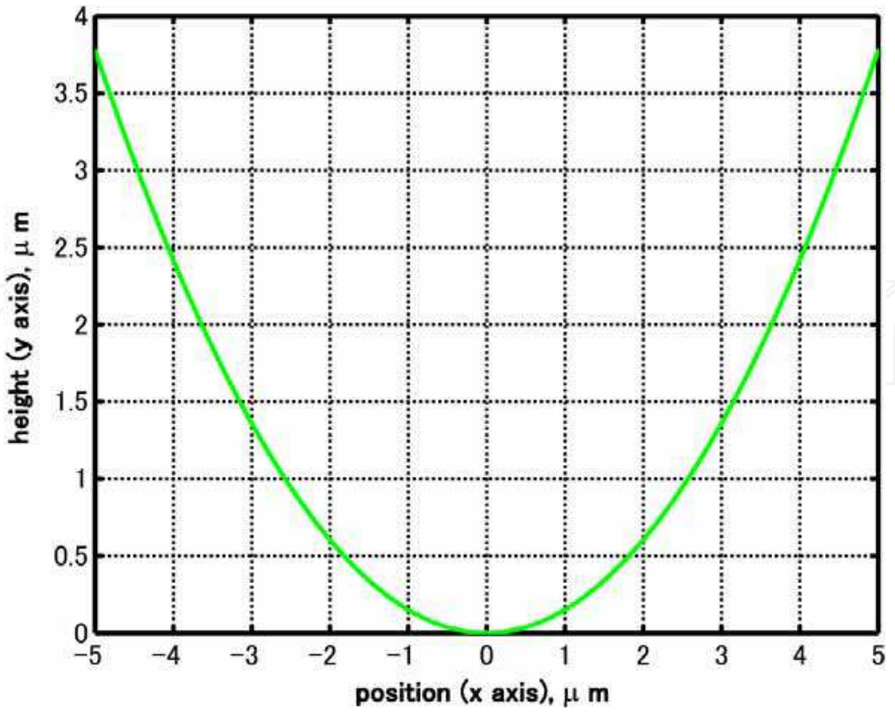

Fig. 9. Convexity model based on measurements: averaged model of five convexities

5. Analysis of sawtoothed feeder surface model

In this study, sawtoothed silicon wafers were applied for feeder surfaces. These surfaces were fabricated by a dicing saw (Disco Corp.), a high-precision cutter-groover using a bevelled blade to cut sawteeth in silicon wafers. Inspecting a sawtoothed silicon wafer using the microscopy system, we obtained a synthesized model (Figure 10) and its contour model (Figure 11). Then we found that these sawtooted surfaces were not perfectly sawtooth shape, but were rounded at the top of sawteeth because of cracks by fabricating errors. So these sawtoothed surfaces were needed to derive surface profile models based on measurements same as Section 4.

Analysing Figure 9 with the DynamicEye Real software, we obtained a numerical model of the top of sawtooth representing with the circle symbol in Figure 12. Defining the feeder coordinate $O-xy$ with the origin O at the maximum value, x axis along the horizontal line, and y axis along the vertical line, this numerical model was approximated with four order polynomials as follows:

$$y = f_s(x) = a_4 x^4 + a_3 x^3 + a_2 x^2 + a_1 x + a_0. \tag{5}$$

An approximation function was drawn with a red continuous line in Figure 11 when each coefficient was defined as Table 1. Interpolating other part of sawtooth with straight lines, we obtained surface profile model of sawtoothed surfaces (Figure 13). In this figure, p shows the sawtooth pitch, and θ shows the angle of elevation. In addition, the incline angle of the line HJ was the same as the angle of elevation θ, the line KL was along the y_s axis, and the curve JK was represented by equation (5).

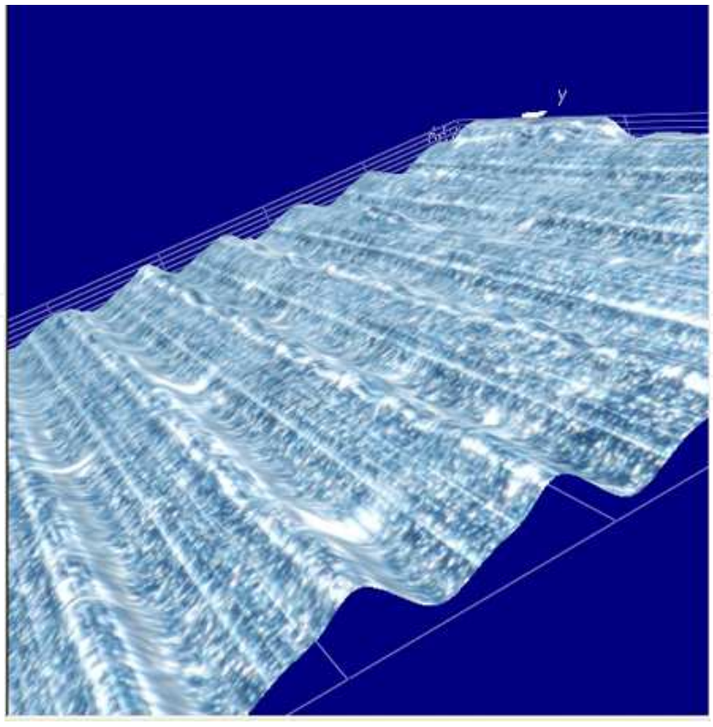

Fig. 10. Synthesized model of sawtoothed surface (p = 0.1 mm and θ=20 deg)

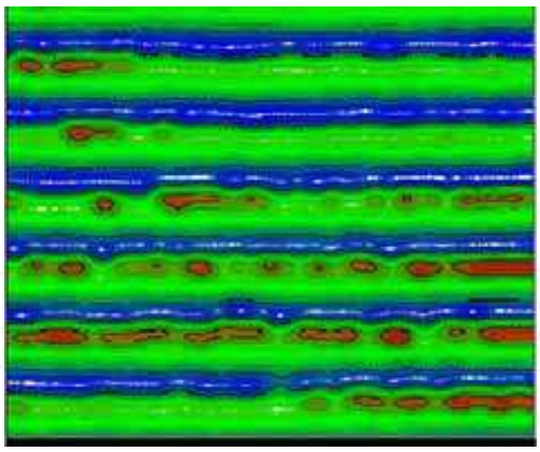

Fig. 11. Contour model

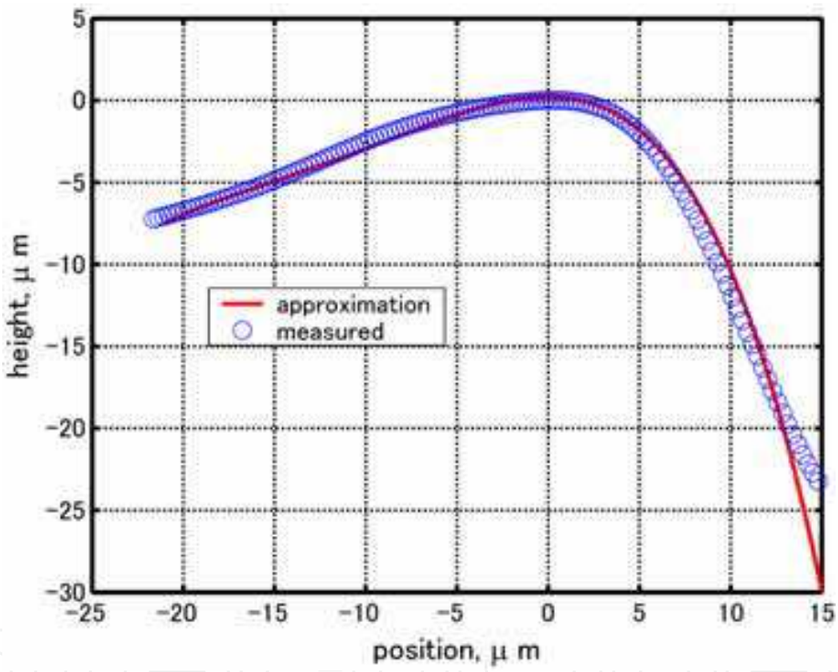

Fig. 12. Measured sawtooth profile and its approximation

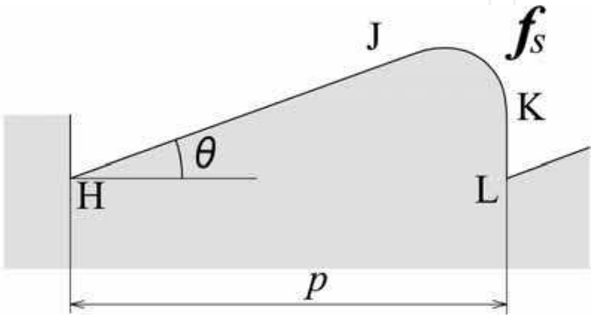

Fig. 13. Surface profile model of sawtooth

a_4	a_3	a_2	a_1	a_0
-0.772e-4	-0.370e-2	-0.611e-1	0.0	0.0

Table 1. Coefficients of approximation function

6. Analysis of contact between approximated models of both surfaces

6.1 Distance between two surfaces

Now we consider contact between two approximation functions represented by equations (2) and (5) as shown in Figure 14. Let us assume that these two functions share a tangent at the contact point $C(x_c, y_c)$, and also assume that adhesion acts perpendicular to the tangent.

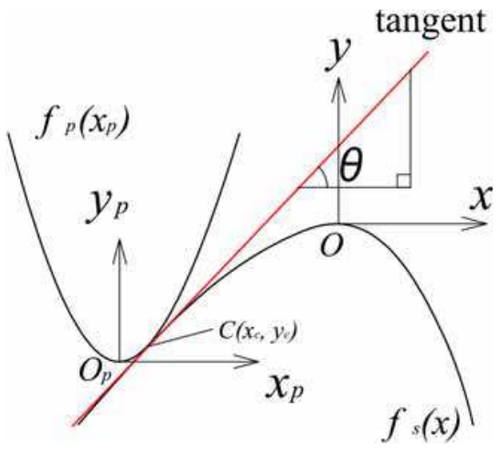

Fig. 14. Contact between two approximation models of micropart and sawtoothed surface

When the part origin O_p is located at ${}^0O_p(x_0, y_0)$ on the feeder coordinate, equation (2) can be rewritten as:

$$y = b(x - x_0)^2 + y_0. \tag{6}$$

Differentiating with respect to x and also substituating the contact point $C(x_c, y_c)$, we have the tangent as follows:

$$y = 2b(x_c - x_0)(x - x_0) + y_c. \tag{7}$$

When the incline of the tangent is defined as $y'(x_c) \equiv \tan\theta$, the following equations are obtained:

$$y'(x_c) = 2b(x_c - x_0) = f_s'(x_c), \tag{8}$$

$$f_s'(x_c) \equiv \frac{df_s(x)}{dx} = 4a_4 {x_c}^3 + 3a_3 {x_c}^2 + 2a_2 {x_c}^1 + a_1. \tag{9}$$

From these equations, the part origin ${}^0O_p(x_0, y_0)$ is calculated as:

$$x_0 = x_c - \frac{f_s^{'}(x_c)}{2b}, \tag{10}$$

$$y_0 = y_c - \frac{\{f_s^{'}(x_c)\}^2}{4b}. \tag{11}$$

Let us consider a normal equation against the tangent passing through a coordinate $Q(x_q, y_q)$. When the normal equation intersects two surfaces at the coorinates $Q_1(x_1, y_1)$ and $Q_2(x_2, y_2)$, respectively (Figure 15), distance of two surfaces can be represented as:

$$dl = Q_1Q_2 = \sqrt{(x_2 - x_1)^2 + (y_2 - y_1)^2}. \tag{12}$$

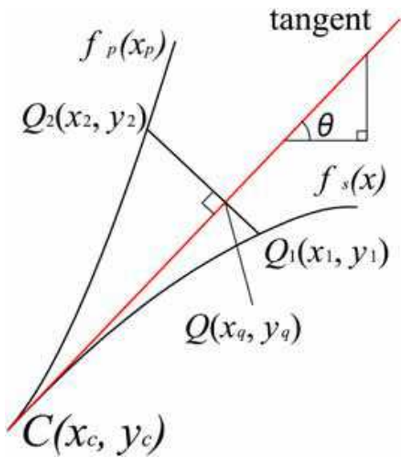

Fig. 15. Distance of two surface models

Now we formulate the coordinate $Q_2(x_2, y_2)$ assuming that the coordinate $Q_1(x_1, y_1)$ is already known. The normal equation is represented as:

$$\begin{cases} y = -\dfrac{1}{y_p^{'}(x_c)}(x - x_1) + y_1 & (y_p^{'}(x_c) \neq 0), \\ x = x_1 & (y_p^{'}(x_c) = 0). \end{cases} \tag{13}$$

Then, substituting into equation (5), we have:

$$x_2 = \begin{cases} x_0\text{-}x_a & (y_p^{'}(x_c) \neq 0), \\ x_1 & (y_p^{'}(x_c) = 0), \end{cases} \tag{14}$$

$$y_2 = \begin{cases} y_0 + b x_a^{\,2} & (y_p^{'}(x_c) \neq 0), \\ y_0 + b(x_1\text{-}x_0) & (y_p^{'}(x_c) = 0), \end{cases} \tag{15}$$

where,

$$x_a \equiv \begin{cases} \dfrac{1}{2b}\left\{\dfrac{1}{y_p'(x_c)} - \sqrt{\dfrac{1}{y_p'(x_c)^2} - 4b\left(\dfrac{x_0 - x_1}{y_p'(x_c)} - (y_0 - y_1)\right)}\right\} & (y_p'(x_c) > 0), \\ \dfrac{1}{2b}\left\{\dfrac{1}{y_p'(x_c)} + \sqrt{\dfrac{1}{y_p'(x_c)^2} - 4b\left(\dfrac{x_0 - x_1}{y_p'(x_c)} - (y_0 - y_1)\right)}\right\} & (y_p'(x_c) < 0). \end{cases} \tag{16}$$

Here, when the square root in equation (16) is imaginary, equations (5) and (13) do not intersect each other, which means that $dl = \infty$.

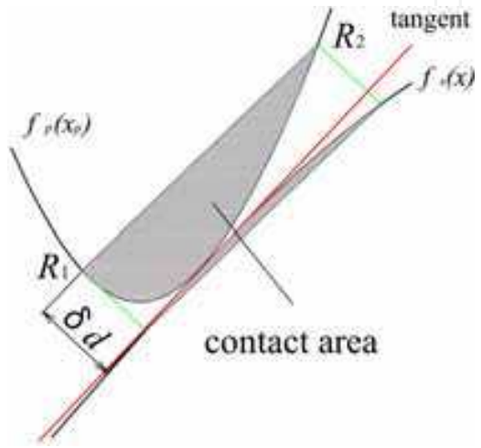

Fig. 15. Definition of contact area

6.2 Area of adhesion

Let as assume that adhesion acts when the distance dl is less than or equal to an adhesion limit δd. In Figure 16, area of adhesion can be defined as colored part between two lines satisfying $dl = \delta d$. Now we defined coordinates R_1 and R_2 as $R_1(x_{r1}, y_{r1})$ and $R_2(x_{r2}, y_{r2})$, (however, $x_{r1} < x_{r2}$), respectively. The equation that passes through R_1 and R_2 is described in the part coordinate system as:

$$y_p = c_r(x_p - x_{r1}) + {x_{r1}}^2, \tag{17}$$

where,

$$c_r = \frac{y_{r2} - y_{r1}}{x_{r2} - x_{r1}}.$$

When equation (17) is applied to the coordinate system $O_p - x_p y_p z_p$ as a plane parallel to the z_p axis, equation (17) cuts the hyperboloid represented in equation (4). In this study, the area of adhesion A is determined by the cut plane as shown in Figure 16. Substituting equation (17) into (4), equation of intersection is obtained:

$$(x_p - \frac{c_r}{2})^2 + {z_p}^2 = (x_{r1} - \frac{c_r}{2})^2. \tag{18}$$

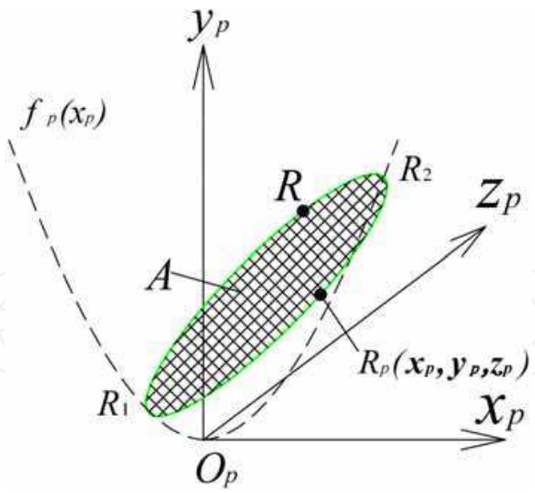

Fig. 16. Area of adhesion

Consequently, we have:

$$A = \pi(x_{r1} - \frac{c_r}{2})^2. \tag{19}$$

Figure 17 show calculation results of area of adhesion, assuming that the adhesion limit δl is determined by the Kelvin equation as follows:

$$\delta l = c_k r_k \equiv -c_k \frac{2\gamma V_m}{\ln \frac{P}{P_0} RT}, \tag{19}$$

where, T is the thermodynamic temperature, R the gas constant, γ the surface tension, P_0 the saturated vapor pressure, P vapor pressure, V_m molecular volume, r_k the Kelvin radius, and c_k proportionally coefficient.

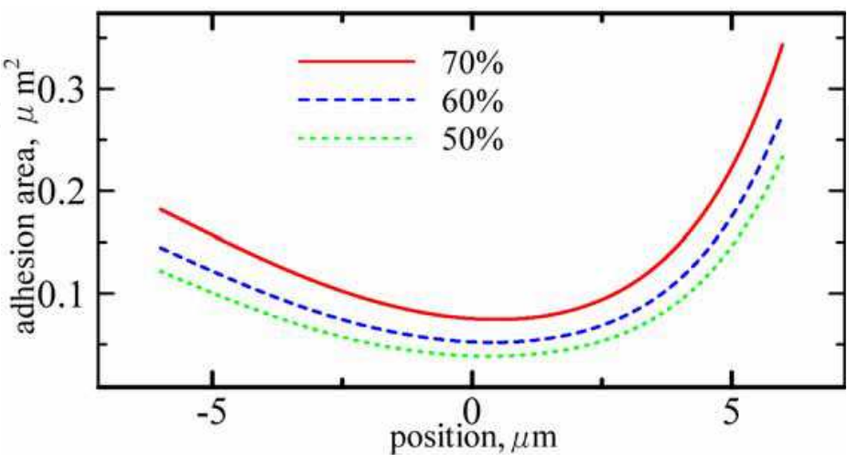

Fig. 17. Area of adhesion

Let F_a, D_A, n, and A_i be the adhesion force, the coefficient of adhesion, number of micropart convexity contacting with the sawtoothed surface, the area of adhesion of i-th

micropart convexity ($i = 1, \cdots, n$), respectively . Assuming that adhesion force is proportional to the area of adhesion, the adhesion force is finally represented as follows:

$$F_a = D_A \sum_{i=1}^{n} A_i , \tag{19}$$

7. Identification of adhesion by angle of friction of microparts

Adhesion between microparts and a feeder surface is affected by surroundings such as temperature and ambient humidity. The Kelvin radius is getting larger as the ambient humidity increases, and then the adhesion force is also getting larger. In this section, we identified the adhesion force based on measurements of angle of friction of microparts under several conditions of ambient humidity.

7.1 Measurements of angle of friction of microparts

Angle of friction of microparts were measured under a temperature of $24^o C$ and an ambient humidity of 50, 60, or 70 %. We prepared sawtoothed silicon wafers with an elevation angle of $\theta = 20^o$ and various sawtooth pitches of $p = 0.01, 0.02, \cdots, 0.1$ mm . Experiments were conducted three times using 35 capacitors. Before experiments, all the experimental equipments were left in the sealed room with keeping constant temperature and ambient humidity for a day.

The averaged experimental data of each experimental condition were plotted in Figures 18 to 20. In these figures, 'positive' direction means that the sawtoothed surface was put as Figure 13, and then was turned around with the clockwise direction, whereas 'negative' direction means when it was turned around with the counter clockwise. Also, the averaged angle of friction at each ambient humidity is shown in Figure 21.

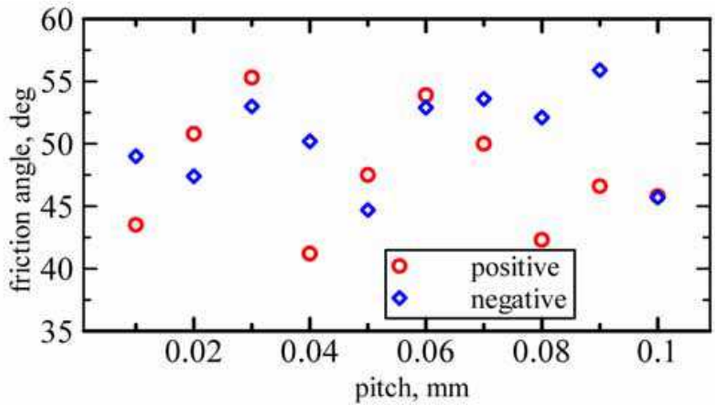

Fig. 18. Angle of friction of microparts with an ambient humidity of 50 %

Now we examine the directionality of friction. From Figures 18 to 20, experimental results at 'positive' direction were totally smaller than that of 'negative' direction, even opposite directions were appeared at on the surfaces of p=0.02, 0.03, 0.05, and 0.06 mm under an ambient humidity of 50 %, and on the surface of p=0.07, 0.08, and 0.09 mm under an ambient humidity of 60 %. The maximum directionality was 17.9 % realized on the surface of p=0.04 mm under an ambient humidity of 50 %, 26.6 % on the surface of p=0.05 mm under an ambient humidity of 60 %, and 15 % on the surface of p=0.06 mm under an

ambient humidity of 70 %. From Figure 21, the angle of friction is getting larger according to ambient humidity, which indicates that the effect of adhesion increases as the increase of ambient humidity.

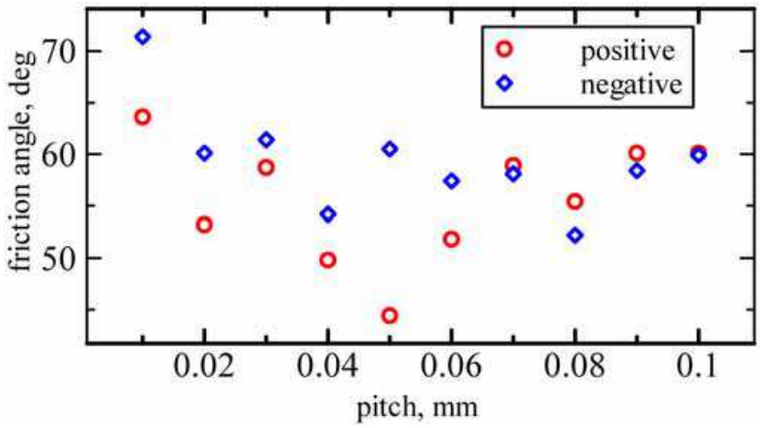

Fig. 19. Angle of friction of microparts with an ambient humidity of 60 %

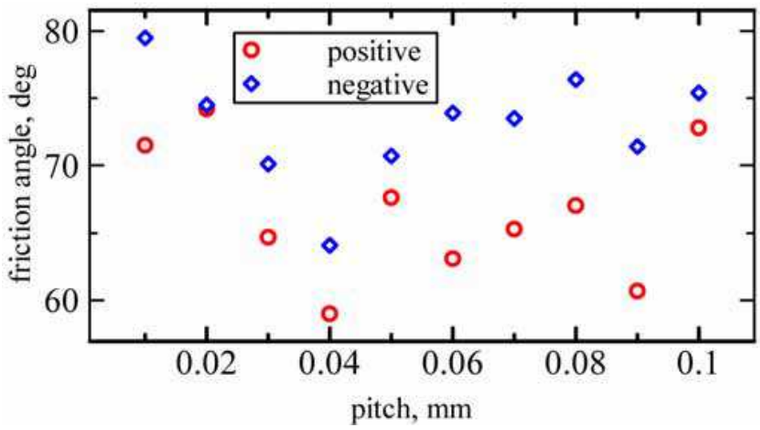

Fig. 20. Angle of friction of microparts with an ambient humidity of 70 %

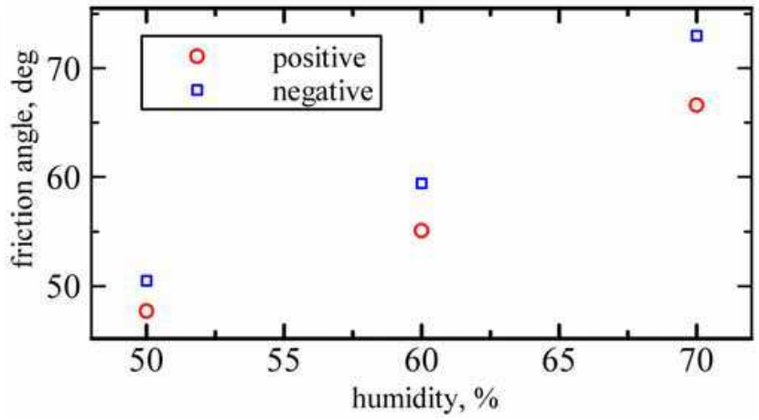

Fig. 21. Relationship between ambient humidity and angle of friction

7.2 Examination of friction coefficient

We consider the case that i-th convexity contacts a sawtooth at a position $x<0$, that is, $\theta_i>0$ (Figure 22). When the surface is inclined to the positive direction, adhesion acts as friction resistance against sliding motion, and also when inclined to the negative direction, adhesion acts as resistance against pull-off force. Let f_{si} be friction resistance against sliding motion, and f_{pi} be resistance against pull-off force, these resistances can be represented as:

$$f_{si}=\mu D_A A_i\cos\theta_i, \tag{20}$$

$$f_{pi}=D_A A_i\sin\theta_i. \tag{21}$$

Similarly, when contact at a position $x>0$ ($\theta_i<0$), these two resistance is rewritten as follows:

$$f_{si}=-\mu D_A A_i\cos\theta_i, \tag{22}$$

$$f_{pi}=D_A A_i\sin\theta_i. \tag{23}$$

On the other hand, when contact occurs at $x=0$ ($\theta_i=0$), adhesion acts as friction resistant against sliding motion according to the direction of incline. If ϕ is the incline of the sawtoothed surface, we have:

$$f_{si}=\begin{cases}-\mu D_A A_i & (\phi<0)\\ \mu D_A A_i & (\phi>0)\end{cases} \tag{24}$$

Let us assume that (m+n) convexities contact sawteeth, then each convexity numbered 1, 2, $\cdots$, m is shared a tangent with $\theta_{pi}>0,(i=1,2,\cdots,m)$, and also each convexity numbered (m+1), (m+2), $\cdots$, (m+n) is shared a tangent with $\theta_{nj}<0,(j=m+1,m+2,\cdots,m+n)$. Let F_p and F_n be the resistances at the positive and negative direction. Also, let A_{pi} and A_{nj} be adhesion area of the i-th convexity and j-th convexity, respectively, we obtained:

$$F_p=D_A\Big(\sum_{i=1}^{m}A_{pi}\sin\theta_{pi}+\mu\sum_{j=1}^{n}A_{nj}\cos\theta_{nj}\Big), \tag{25}$$

$$F_n=D_A\Big(\mu\sum_{i=1}^{m}A_{pi}\cos\theta_{pi}-\sum_{j=1}^{n}A_{nj}\sin\theta_{nj}\Big). \tag{26}$$

When the incline of the feeder surface is ϕ, inertia of micropart along the feeder surface is represented as:

$$F(\phi)=mg\sin\phi-\mu mg\cos\phi, \tag{27}$$

where, m is mass of micropart and g is gravity. Let as assume that micropart starts to move when the resistance caused by adhesion balances the inertia of micropart, $F(\phi)$. If ϕ_p and ϕ_n are angles of friction of positive and negative direction, respectively, we have:

$$F_p=mg\sin\phi_p-\mu mg\cos\phi_p, \tag{28}$$

$$F_n = mg\sin\phi_n - \mu mg\cos\phi_n. \tag{29}$$

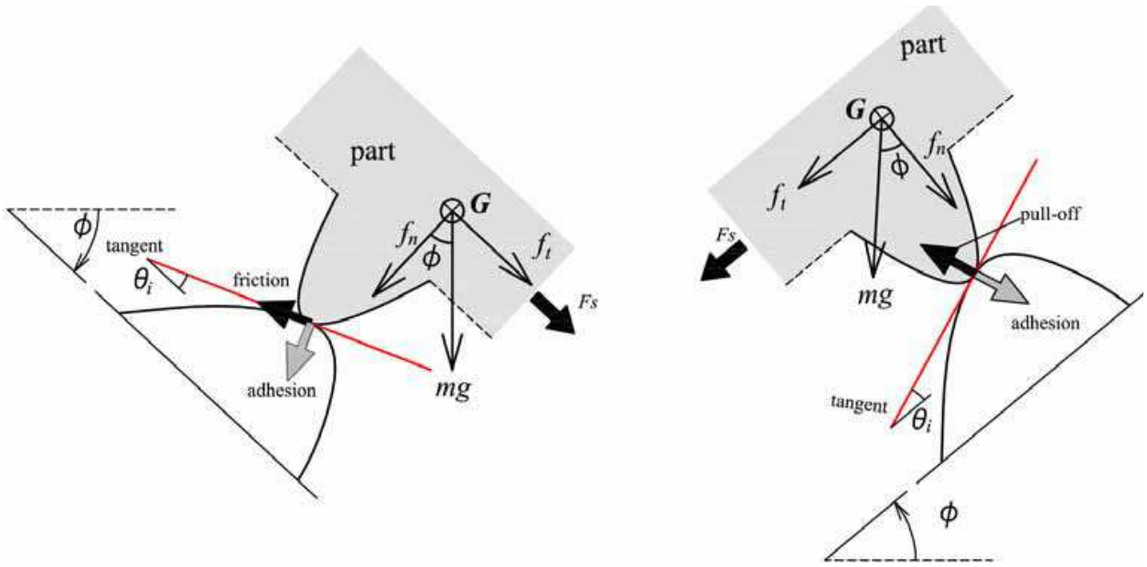

Fig. 22. Resistance caused by adhesion

7.3 Identification of friction and adhesion

First, we identified the coefficient of friction from experimental results in Figure 21. Assuming that adhesion is proportional to area adhesion, we decided the ratio of adhesion according to ambient humidity from Figure 17 as follows:

$$\frac{A_{(dir)}(60\%)}{A_{(dir)}(50\%)} = \frac{F_{(dir)}(60\%)}{F_{(dir)}(50\%)} = 1.18, \frac{A_{(dir)}(70\%)}{A_{(dir)}(50\%)} = \frac{F_{(dir)}(70\%)}{F_{(dir)}(50\%)} = 1.47, \tag{30}$$

where, either symbol 'p' or 'n' is substituted into the subscript '(dir)' according to direction. Substituting m=0.3 mg and g = 9.8 m/s² into equations (28) and (29), we identified the coefficient of friction so as to fit equation (30). From Figure 23, the identification results when $\mu = 0.28$ corresponds with simulations, error between both results is 0.96 %.

Next, we considered the identification of adhesion. In equations (25) and (26), we assumed that:

$$m = n, \tag{31}$$

$$\sum_{i=1}^{n} A_{(dir)i}\sin\theta_{(dir)i} \equiv A_{(dir)0}\sin\theta_{(dir)0}, \tag{32}$$

$$\sum_{i=1}^{n} A_{(dir)i}\cos\theta_{(dir)i} \equiv A_{(dir)0}\cos\theta_{(dir)0}. \tag{33}$$

Substituting equations (31), (32) and (33) into equations (25) and (26), we have:

$$F_p = D_A(A_{p0}\sin\theta_{p0} + \mu A_{n0}\cos\theta_{n0}), \tag{34}$$

$$F_n = D_A(\mu A_{p0}\cos\theta_{p0} - A_{n0}\sin\theta_{n0}). \tag{35}$$

Then, the ratio of adhesion of positive and negative direction was formulated as:

$$\frac{F_p}{F_n} = \frac{A_{p0}\sin\theta_{p0} + \mu A_{n0}\cos\theta_{n0}}{-A_{n0}\sin\theta_{n0} + \mu A_{p0}\cos\theta_{p0}}. \tag{36}$$

Substituting the ratio of adhesion calculated from equations (28) and (29) into equation (36), we identified variables $A_{(dir)0}$ and $\theta_{(dir)0}$ (Table 2). Consequently, the coefficient of adhesion was almost constant while there was 4 % error at each ambient humidity condition. We finally decided $D_A = 3.72\times10^2\ \mu N/\mu m^2$ averaging them.
To assess the identified results, we compared experiments with calculation using the identified results. From Figure 24, identification results were in well agreement with experiments.

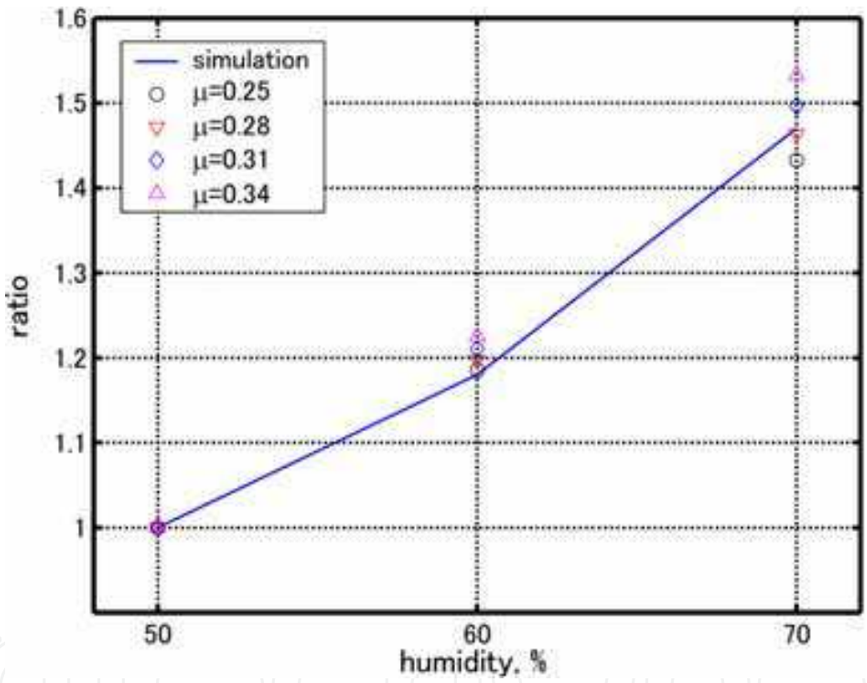

Fig. 23. Identification of coefficient of friction

7.4 Micropart dynamics including adhesion

When the feeder surface moves with sinusoidal vibration at an amplitude A_{vib} and an angular frequency ω (Figure 25), the inertia F_s transffered to a micropart is defined according to relative motion of the micropart and the feeder surface and its contact position as follows:

$$\begin{aligned} F_{vib} &= -mAvib\omega^2\sin\omega t, \\ F_s &= \begin{cases} F_{vib}\sin^2\theta & (\theta \neq 0) \\ 0 & (\theta = 0) \end{cases} \end{aligned} \tag{37}$$

ambient humidity	50 %	60 %	70 %
x_c, μm	±0.913		
θ_{p0}, rad	0.102		
θ_{n0}, rad	–0.121		
A_{p0}, μm^2	$1.21e-2$	$1.42e-2$	$1.77e-2$
A_{n0}, μm^2	$1.12e-2$	$1.32e-2$	$1.65e-2$
D_A, $\mu N / \mu m^2$	$3.63e+2$	$3.80e+2$	$3.72e+2$

Table 2. Identification of adhesion

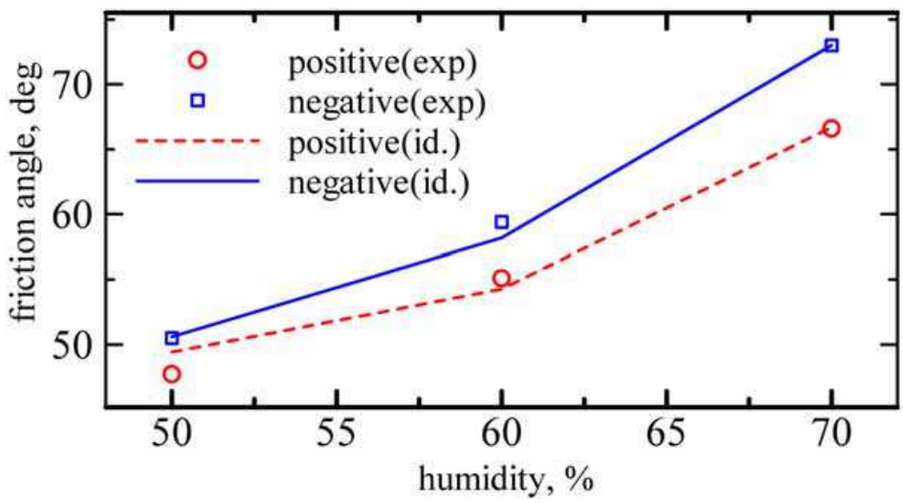

Fig. 24. Comparison of identfication and experiments

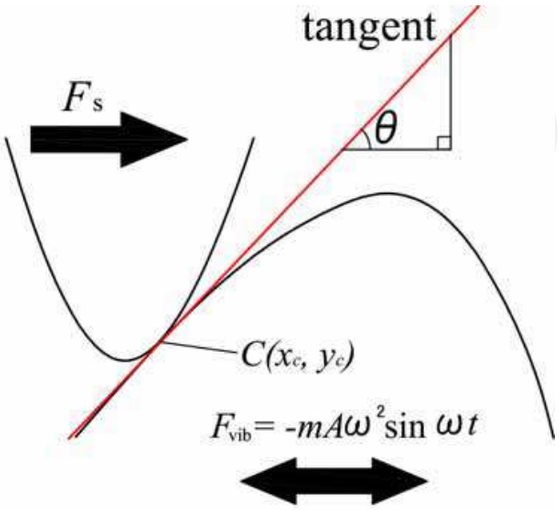

Fig. 25. Transferred force from feeder surface to micropart

Also, If x_p is micropart position, micropart dynamics is given by:

$$F_s = m\ddot{x}_p + c\dot{x}_p, \tag{38}$$

where, c is the coefficient of viscous attenuation, $\ddot{x}_p$ second order time differential, and $\dot{x}_p$ time differential.

Next we considered the effect of adhesion. Adhesion changes according to the relative motion of micropart on the feeder surface. If *x* is displacement of the feeder surface, velocity of the feeder surface is represented as:

$$\dot{x} = \frac{dx}{dt} = \omega A_{vib} \cos \omega t, \tag{39}$$

Then the micropart dynamics along the x axis can be expressed as:

$$m\ddot{x}_p + c\dot{x}_p = F_s - F_{(dir)}, \tag{40}$$

where,

$$F_{(dir)} = \begin{cases} F_p & (\dot{x}_p - \dot{x} > 0) \\ F_n & (\dot{x}_p - \dot{x} < 0) \end{cases}$$

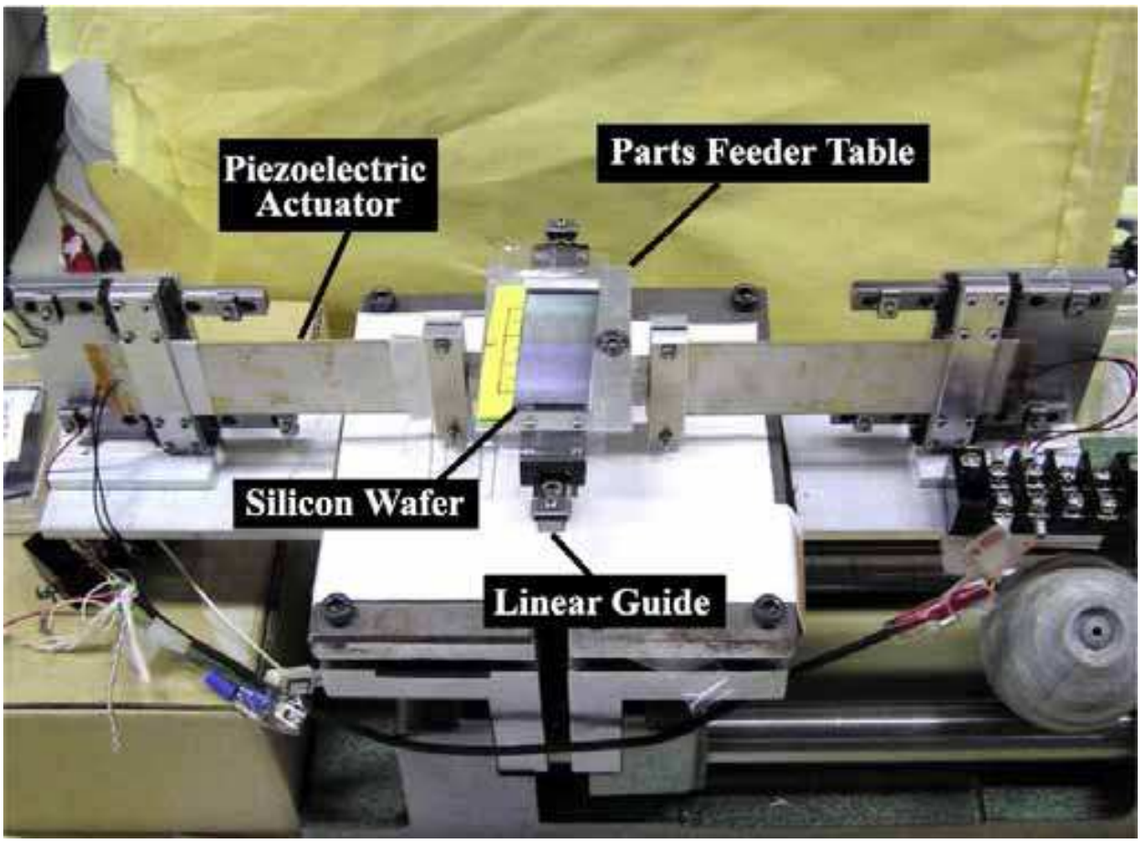

Fig. 26. Microparts feeder using bimorph piezoelectric actuators

8. Feeding experiments of micropart

8.1 Experimental equipment

In micropart feeder (Figure 26), a sawtoothed silicon wafer is placed at the top of the feeder table, which is driven back and forth in a track by a pair of piezoelectric bimorph elements, powered by a function generator and an amplifier that delivers peak-to-peak output voltage of up to 300 V.

8.2 Feeding experiments

Using this microparts feeder and sawtoothed silicon wafers mentioned in section 7.2, we conducted feeding experiments of microparts at a frequency of f=98 to 102 Hz with an interval of 0.2 Hz, and at an amplitude of A=0.5 mm under an ambient humidity of 60 % and a temperature of 24°C.

Each experimental result is the average of three trials using five microparts. Then the maximum feeding velocities of each feeder surface was recorded in Table 3.

When the pitch was 0.04 mm or less, the velocity was around 0.6 mm/s at a driving frequency f=98 to 100 Hz. The fastest feeding was 1.7 mm/s which was realized at a frequency f=101.4 Hz on p=0.05 mm surface. When the pitch was 0.06 mm or larger, the maximum velocities were around 1.0 mm/s at a frequency around f=101.4 Hz.

pitch, mm	velocity, mm/s	frequency, Hz
0.01	0.695	99.2
0.02	0.839	98.8
0.03	0.749	100.0
0.04	0.582	99.2
0.05	1.705	101.4
0.06	0.880	101.6
0.07	1.253	101.4
0.08	1.262	101.8
0.09	0.883	101.2
0.10	1.049	101.6

Table 3. Maximum feeding velocity on each feeder surface

8.3 Comparison of feeding simulation

Using equations (37) and (40), we simulated microparts feeding with the same conditions as experiments. In order to assess the effectiveness of adhesion, we conducted simulations when adhesion would be ignored. Experimental results and both simulation results were plotted simultaneously (Figure 27).

From this figure, both simulations were far from experimental results. These differences were caused by rotational motion around the axis along the sawtooth groove (Mitani, 2007).

9. Conclusion

We formulated feeding dynamics of microparts considering the effect of adhesion between sawtoothed silicon wafers and capacitors. Using a microscopy system, we obtained precise surface models of a micropart and sawtoothed silicon wafers. Contact between two surface models was analysed assuming that they shared a tangent at the contact point. Adhesion was then examined according to adhesion limit that both surfaces are near enough to adhere each other. Experiments of angle of friction of microparts were conducted in order to identify the coefficients of friction and adhesion. The feeding dynamics including the effect of adhesion were finally formulated.

Comparing simulation using the dynamics derived and experimental results, we found large differences between them because of rotation around the axis along to sawtooth groove.

In future studies, we will try to:

- Identify micropart dynamics including rotation, and
- Develop feeder surfaces with more precise profile.

This research was supported in part by a Grant-in-Aid for Young Scientists (B) (20760150) from the Ministry of Education, Culture, Sports, Science and Technology, Japan, and by a grant from the Electro-Mechanic Technology Advancing Foundation (**EMTAF**), Japan.

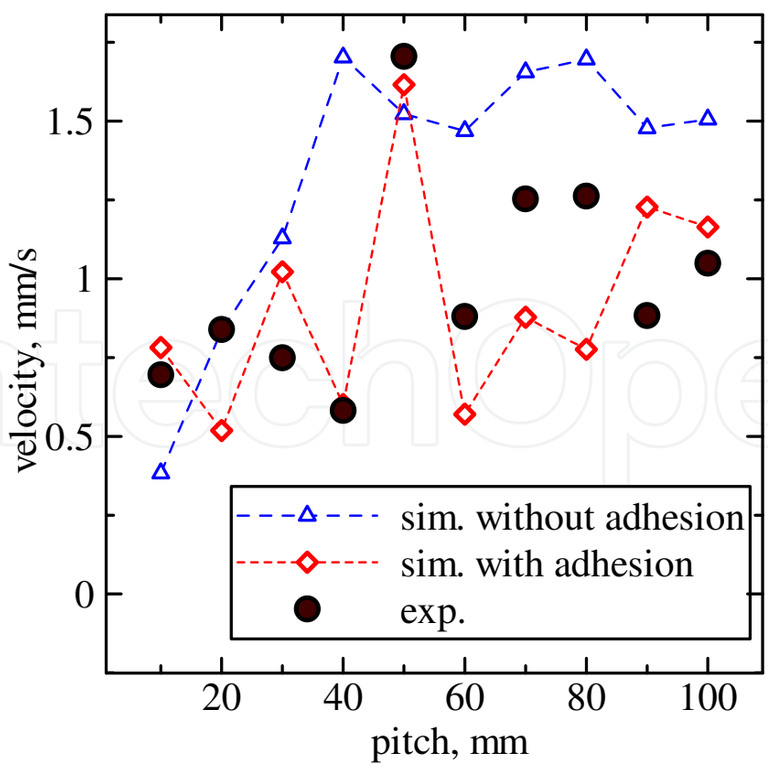

Fig. 27. Comparison of feeding experiments and simulations

10. References

Mitani, A., Sugano, N. & Hirai, S.(2006). Micro-parts Feeding by a Saw-tooth Surface, *IEEE/ASME Transactions on Mechatronics*, Vol. 11, No. 6, 671-681.

Ando, Y. & Ino, J. (1997). The effect of asperity array geometry on friction and pull-off force, *Transactions of the ASME Journal of Tribology*, Vol. 119, 781-787.

Maul, G. P. & Thomas, M. B. (1997). A systems model and simulation of the vibratory bowl feeder, *Journal of Manufacturing System*, Vol. 16, No. 5, 309-314.

Wolfsteiner, P. & Pfeiffer, F. (1999). The parts transportation in a vibratory feeder, *Procs. IUTAM Symposium on Unilateral Multibody Contacts*, 309-318.

Reznik, D. & Canny, J. (2001). C'mon part, do the local motion!, *Procs. 2001 International Conference on Robotics and Automation*, Vol. 3, 2235-2242.

Berkowitz, D.R. & Canny, J. (1997), A comparison of real and simulated designs for vibratory parts feeding, *Procs. 1997 IEEE International Conference on Robotics and Automation*, Vol. 3, 2377-2382.

Christiansen, A. & Edwards, A. & Coello, C. (1996). Automated design of parts feeders using a genetic algorithm, *Procs. 1996 IEEE International Conference on Robotics and Automation*, Vol. 1, 846-851

Doi, T, (2001), Feedback control for electromagnetic vibration feeder (Applications of two-degrees-of-freedom proportional plus integral plus derivative controller with nonlinear element), *JSME International Journal*, Series C, Vol. 44, No. 1, 44-52.

Konishi, S. (1997). Analysis of non-linear resonance phenomenon for vibratory feeder,
Procs. APVC '97, 854-859.

Fukuta, Y. (2004). Conveyor for pneumatic two-dimensional manipulation realized by arrayed MEMS and its control, *Journal of Robotics and Mechatronics*, Vol. 16, No. 2, 163-170.

Arai, M (2002). An air-flow actuator array realized by bulk micromachining technique, *Procs. IEEJthe 19th Sensor Symposium*, 447-450.

Ebefors, T. (2000), A robust micro conveyer realized by arrayed polyimide joint actuators, *Journal of Micromechanics and Microengineering*, Vol. 10, 337-349.

Böhringer, K.-F. (2003). Surface modification and modulation in microstructures: controlling protein adsorption, monolayer desorption and micro-self-assembly, *Journal of Micromechanics and microengineering*, Vol. 13, S1-S10.

Oyobe, H. & Hori, Y. (2001). Object conveyance system "Magic Carpet" consisting of 64 linear actuators-object position feedback control with object position estimation, *Procs. 2001 IEEE/ASME International Conference on Advanced Intelligent Mechatronics*, Vol. 2, 1307-1312.

Fuhr, G. (1999), Linear motion of dielectric particles and living cells in microfabricated structures induced by traveling electric fields, *Procs. 1999 IEEE Micro Electro Mechanical Systems*, 259-264.

Komori, M. & Tachihara, T. (2005). A magnetically driven linear microactuator with new driving method, *IEEE/ASME Transactions on Mechatronics*, Vol. 10, No. 3, 335-338.

Ting, Y. (2005), A new type of parts feeder driven by bimorph piezo actuator, *Ultrasonics*, Vol. 43, 566-573.

Codourey, A. (1995). A robot system for automated handling in micro-world, *Procs. 1995 IEEE/RSJ International Conference on Intelligent Robots and Systems*, Vol. 3, 185-190.

Mitani, A. & Hirai, S. (2007) Feeding of Submillimeter-sized Microparts along a Saw-tooth Surface Using Only Horizontal Vibration: Analysis of Convexities on the Surface of Microparts, Procs. IEEE 2007 3rd Conference on Automation Science and Engineering (CASE2007) , Scottsdale , AZ , USA, Sep. 22-25, 2007.

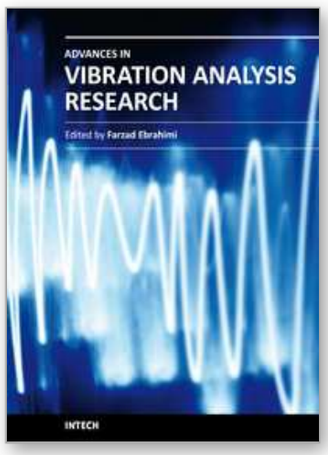

Advances in Vibration Analysis Research

Edited by Dr. Farzad Ebrahimi

ISBN 978-953-307-209-8
Hard cover, 456 pages
Publisher InTech
Published online 04, April, 2011
Published in print edition April, 2011

Vibrations are extremely important in all areas of human activities, for all sciences, technologies and industrial applications. Sometimes these Vibrations are useful but other times they are undesirable. In any case, understanding and analysis of vibrations are crucial. This book reports on the state of the art research and development findings on this very broad matter through 22 original and innovative research studies exhibiting various investigation directions. The present book is a result of contributions of experts from international scientific community working in different aspects of vibration analysis. The text is addressed not only to researchers, but also to professional engineers, students and other experts in a variety of disciplines, both academic and industrial seeking to gain a better understanding of what has been done in the field recently, and what kind of open problems are in this area.

InTech Europe
University Campus STeP Ri
Slavka Krautzeka 83/A
51000 Rijeka, Croatia
Phone: +385 (51) 770 447
Fax: +385 (51) 686 166
www.intechopen.com

InTech China
Unit 405, Office Block, Hotel Equatorial Shanghai
No.65, Yan An Road (West), Shanghai, 200040, China
中国上海市延安西路65号上海国际贵都大饭店办公楼405单元
Phone: +86-21-62489820
Fax: +86-21-62489821

IntechOpen